Motion Compensation in High Frame Contrast Enhanced Ultrasound Imaging

João Miguel Gomes Ribeiro
Instituto Superior Técnico
joao.miguel.gomes.ribeiro@tecnico.ulisboa.pt

Abstract - High frame rate ultrasound imaging using coherent compounding of unfocused transmissions acquired at different angles has been shown to greatly improve image quality and frame rate when compared to conventional methods. By using microbubble contrast agents and coded transmissions (such as PI or AM), this technique can be used to image blood vessels and the heart and its flow dynamics. However, the coherent compounding method suffers greatly from motion artefacts. While motion compensation methods have been developed and successfully integrated with coherent compounding, a motion compensation scheme specific for contrast enhanced ultrasound imaging has not yet been developed. Within this scope, this work investigated a Doppler-based motion compensation scheme with the purpose of optimizing it for high frame rate contrast enhanced ultrasound imaging. Two distinct transmit sequences were investigated and incorporated with PI/AM: angled multipulse contrast, where all coded transmission pulses are acquired at the same angle, and alternated contrast, where the coded transmission is integrated directly in the angle sequence. Motion compensation schemes were developed for both types of transmission sequences to determine the optimal method to compensate motion in contrast mode.

I. Introduction

ULTRASOUND (US) imaging is a noninvasive, easily portable, and relatively inexpensive diagnostic modality which finds extensive use in the clinic [1]. Operating typically at frequencies between 1 and 10 MHz, it produces images via the backscattering of mechanical energy - sound - from boundaries between tissues and from small structures within tissue.

Conventionally, images in US are acquired "line-by-line" by transmitting narrow focused beams. Using this conventional method, ultrasound has the capability of real-time imaging at up to 30 frames per second. There are many phenomenons in the human body that benefit from being imaged in real-time and for which frame rates at the order of 30 frames per second is insufficient. One such example is the heart, where the imaging of contractions and blood flows are greatly benefited by increasing the temporal resolution, while the very fast opening and closing of the mitral leaflets is simply not possible to observe using such low frame rates.

Nowadays, there exist methods to acquire US images at up 10 000 frames per second by using unfocused transmissions. These high frame rate (HFR) methods rely on coherent compounding of multiple transmissions acquired in slightly different directions to achieve sufficiently high signal-to-noise ratio (SNR) [2, 3]. Apart from the massive increase in frame rate, image quality in coherent compounding US imaging is in many aspects better than conventional US.

The one disadvantage of compounding to improve image quality is that it requires that the locations of the scatterers present in the imaged medium remain static during acquisition. Whenever that is not the case, significant motion artefacts are observed [4].

Motion compensation (MoCo) is often employed in HFR US imaging to eliminate motion artefacts, especially in echocardiography, where large motions are observed [5].

Despite the improved image quality obtained in HFR US imaging, there are many situations in which coherent compounding is not enough to achieve sufficiently high signal of the imaged medium. That occurs more notably in the presence of small blood vessels since erythrocytes are weak ultrasound scatterers and their signal is masked by the surrounding tissue signal [6]. To improve the level of signal from blood flows, gas-filled microbubble contrast agents are often used. The scattering cross-section of microbubbles is extremely high due to the gas-liquid boundary. Additionally, scattering through microbubbles is largely nonlinear and thus these produce high harmonic content [7], contrary to tissue which produces mostly linear signal.

Contrast-enhanced ultrasound imaging (CEUS) with microbubbles is commonly combined with multipulse methods. The purpose of multipulse methods is to subtract consecutive transmissions, eliminating the linear tissue signal while retaining the nonlinear microbubble signal. Pulse Inversion (PI) and Amplitude Modulation (AM) are the most widely used multipulse coded transmission sequences in ultrasound imaging and both provide high-contrast images of blood vessels.

CEUS has been integrated with coherent compounding to achieve HFR high-contrast images [8, 9]. However, research on the optimal way of integrating coded transmission with coherent compounding is lacking. Furthermore, motion compensation schemes specific for HFR CEUS are extremely under investigated.

Doppler-based motion compensation methods provide a computationally inexpensive approach to compensate axial motion. However, despite these methods being quite developed for general HFR imaging, they are yet to be optimized for HFR CEUS.

This work intends to investigate Doppler-based motion compensation schemes in HFR CEUS using coded transmission - PI and AM. The main objective is to adapt the Doppler autocorrelator approach developed for HFR imaging [10] to CEUS in both PI and AM sequences, as well as optimizing the pulse sequences in terms of the accuracy of the MoCo method.

As an initial evaluation of Doppler MoCo methods in HFR CEUS, developing a framework where the results are reproducible and the ground truths are known is key. With

that in mind, a study fully on simulation data was developed. The findings on simulation data, for which the parameters of the medium and the acquisition are known fully, are able to be translated to real acquisitions, taking potential limitations into account.

II. Methods

A. Phantom design

Doppler-based MoCo methods are only capable of correcting axial motions. Having a wide range of axial velocities is hence valuable. Rotation motions in circular objects are ideal for axial velocity evaluation for two reasons: 1. The magnitude of the velocity increases linearly radially from the center; 2. The direction of the velocity is always perpendicular to the distance vector from the center. These two properties combined create an axial velocity profile that linearly increases in the lateral direction from the maximum negative velocity to the maximum positive velocity, passing by zero at the center. Additionally, for each axial direction line the velocity is constant across all depths.

On another note, because loss of contrast is common in motion degraded images due to coherent compounding, having both anechoic and hyperechoic regions will provide a way to compare contrast recovery in motion compensated images.

The phantom that was modeled to evaluate a wide range of velocities and contrast recovery was a rotating disc with anechoic inclusions. This type of phantom has been previously evaluated in other motion estimation and compensation studies, albeit in-vitro and not in simulation [10–12]. The properties of the disc are summarized in Table I.

TABLE I
SUMMARY OF PROPERTIES OF THE ROTATING DISC PHANTOM

	Disc	Cysts / Background
Radius	2.5 cm	0.375 cm
B/A [13–16]	1000	6
Sound speed [16]	1540 $\pm$ 15.4 m/s	1540 $\pm$ 0.77 m/s
Attenuation coefficient [16]	0.56 dB/(MHz cm)	
Angular velocity	12 rad/s	
Medium size	10 $\times$ 10 cm	

With the described parameters, the rotating disc phantom looks like the one presented in Figure 1.

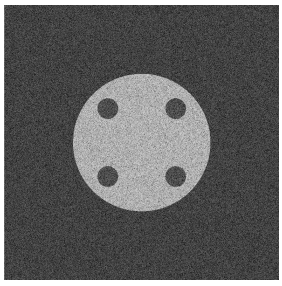

Fig. 1. Rotating disc phantom as a sound speed map. Higher variations from the reference sound speed c_0 result in increased brightness. This figure was generated in reference to deviations from the mean acoording to $|c_{ij} - c_0|$.

B. Transmit sequences in contrast mode

One of the ways multipulse contrast imaging can be integrated with coherent compounding is acquiring two/three pulses per angle for PI/AM, respectively. Figure 2 shows this transmission sequence for the case of pulse inversion using diverging waves.

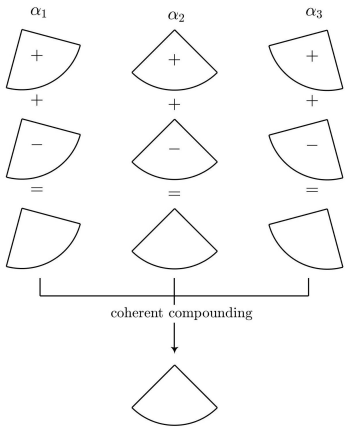

Fig. 2. Coherent compounding with multiple pulses per angle and pulse inversion. For each angle α, two consecutive pulses in opposite phase are transmitted. These are summed to get a higher-contrast LRI, and only then are the LRIs summed for a coherently compounded image.

The provided example is for PI, but the same principle can be applied to AM.

A different way to acquire contrast images is by integrating the coded transmissions directly in the angle sequence. For PI, that would be transmitting the first angle as a positive pulse and the second angle as a negative pulse, and so on. This imposes the condition of the number of angles being a multiple of two for PI and a multiple of three for AM. Figure 3 illustrates a typical alternated angle contrast sequence using pulse inversion and diverging waves.

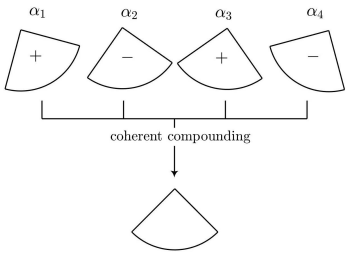

Fig. 3. Coherent compounding with alternated angle pulse inversion. For each angle α, a single positive or negative pulse is transmitted. The phase of each angled transmission is alternated.

To differentiate between the two types of transmissions, the names angled multipulse contrast and alternated contrast are introduced. The name "contrast" can be substituted by the appropriate technique, namely PI and AM - angled multipulse PI/AM (MultiPI/MultiAM) and alternated PI/AM (AltPI/AltAM).

C. Simulations

Ultrasound propagation simulations were performed using k-Wave for its ability to simulate nonlinear propagation

[17, 18]. Diverging wave transmissions were used to image the medium phantom described earlier. Simulations were performed at three different transmit frequencies to evaluate the effect of the transmit frequency in motion compensation. The parameters of the simulated acquisition are summarized in Table II:

TABLE II
SUMMARY OF SIMULATION PARAMETERS USING DIVERGING WAVES.

Property	Value
Transmit frequency (cycles)	1.25/ 1.75/ 2.50 MHz (4)
Number of angles	12
Angle step [4]	2.53°/1.81°/1.26°

Simulations with given properties were performed for both types of transmission sequences and for both PI and AM. The same simulations were repeated for the disc in static conditions to serve as a positive control for motion compensation.

D. Motion estimation and compensation

1) The Doppler autocorrelator

The Doppler effect can be described as a frequency shift due to the relative motion between the emitter and the scatterer. In pulsed transmissions, in contrast with continuous ones, determining the frequency shift directly is challenging because of the short duration of the pulses. Instead, if the motions are small enough, the frequency shift can be determined indirectly from the phase shifts between pulses, which themselves can be determined from a lag-one autocorrelator, also typically named the Doppler autocorrelator.

Given a signal $s(x, z, n)$, where the third coordinate represents discrete time to denote each acquisition, the Doppler autocorrelator is given by:

$$r_D = \sum_{n=0}^{N-2} s(n)s^*(n+1) \tag{1}$$

where the space coordinate dependence has been made implicit. From Kasai et al. (1985), the signals must be I/Q demodulated at the transmit frequency to for correct phase estimates. Substituting $s(n)$ by the respective I&Q components, $s(n) = I(n) + jQ(n)$:

$$r_D = \sum_{n=0}^{N-2} (I(n) + jQ(n))(I(n+1) + jQ(n+1))^* \tag{2}$$

By separating the real and imaginary components of the autocorrelator, the phase of the lag-one autocorrelator is given by:

$$\begin{aligned} \phi_D &= \arctan \frac{\mathrm{Im}\{r_D\}}{\mathrm{Re}\{r_D\}} \\ &= \arctan \frac{\sum_{n=0}^{N-2} Q(n)I(n+1) - I(n)Q(n+1)}{\sum_{n=0}^{N-2} I(n)I(n+1) + Q(n)Q(n+1)} \end{aligned} \tag{3}$$

Equation 3 is a close-form approximated solution to the Doppler phase-shift. The axial velocity of the scatterers that produce the phase shifts can be computed using the Doppler phase equation [16]:

$$v_D = \frac{c\mathrm{PRF}\phi_D}{4\pi f_0} \tag{4}$$

2) Doppler motion compensation

Motion compensation in coherent compounding aims at estimating motion between LRIs and correcting each of them before summation, ensuring coherence.

Given a set of N LRIs, each acquired with an unfocused transmission at a different transmit angle, the axial velocity can be estimated using equations 3 and 4. The axial velocity is estimated with the assumption that the phase of the autocorrelator remains constant during a pulse repetition period, which is equivalent to saying that the axial velocity profile remains constant throughout the acquisition. Using this approximation, the axial displacement amplitude is itself constant between acquisitions and is given by the product of the axial velocity and the time between each acquisition:

$$u_D = \frac{v_D}{\mathrm{PRF}} = \frac{c\phi_D}{4\pi f_0} \tag{5}$$

Under the same assumption, the motion between one LRI and a different LRI in the same sequence is an integer multiple of u_D. There are two steps to ensure a coherent sum [4]:

1) Axial displacement compensation;
2) Phase correction.

By picking one of the LRIs for reference, such as the middle one, axial displacement compensation can be performed as a spatial shift in the axial coordinate, z, and the phase correction as a product with a complex exponential of the Doppler phase shift. Compounding with built-in MoCo can be written in the form:

$$S(x, z) = \sum_{n=0}^{N-1} s\left(x, z + \left(n - \frac{N}{2}\right) u_D, n\right) e^{jn\phi} \tag{6}$$

E. Multiple angle transmit sequence ordering

The ordering of the transmit sequence has a significant impact on the coherently compounded images [4, 10]. Because a triangular transmit sequence ordering suppresses sidelobes the most, that is the sequence that is used. The triangular sequence can be interpreted as two consecutive sequences of angles: the first one ascending and the second one descending. If the angles [-10, -6, -2, 2, 6 10] were to be used, they would be reordered as [-10, -2, 6, 10, 2, -6], such that the first half is increasing and the second half decreasing. This ordering is preferential for Doppler MoCo schemes, as side lobe influence is suppressed during motion estimation [10]. Motion estimation is adjusted by using one lag-one autocorrelator for the ascending sequence of images and another one for the second sequence. The estimated Doppler phase shift is the mean of the ascending and descending autocorrelator phases. A disadvantage of this approach is that aliasing occurs at half

the classical Doppler velocity limit, making this methodology more prone to aliasing.

F. Compensation in contrast mode

1) Motion compensation in angled multipulse contrast mode

Given the pulse sequence of angled multipulse contrast mode, there are three possibilities for Doppler MoCo between LRIs:

1) Sum the contrast pulses without compensating and compensate motion only between the angled transmissions - MoCo C;
2) Compensate between contrast pulses, sum them, and then compensate the resulting angled transmissions separately - MoCo B;
3) Compensate between all the LRIs directly - MoCo A.

The letter notation (i.e., MoCo A/B/C) is introduced to refer to each motion compensation scheme in a more compact form. Figures 4-6 show the simplified pipelines of the motion compensation schemes.

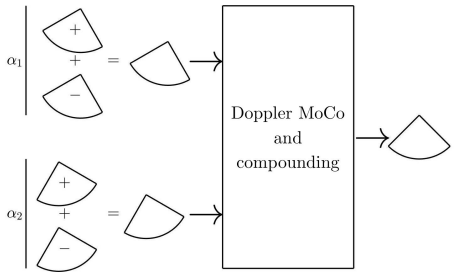

Fig. 4. MoCo C: The coded transmission pulses are summed and compensation is performed between the compounding angles.

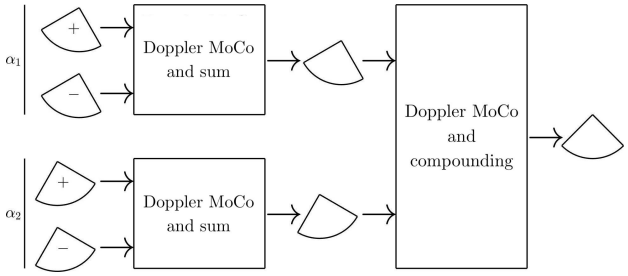

Fig. 5. MoCo B: Motion is compensated between coded transmission pulses and then between the compounding angles.

2) Motion compensation in alternated contrast mode

The alternated contrast mode sequence can be treated as a non-contrast sequence and compensated using Doppler MoCo. Since coded transmission is embedded directly in the angle sequence, no additional processing is required. Figure 7 summarizes the motion compensation pipeline.

G. Evaluation metrics

Images were envelope-detected and log-compressed for display purposes. A dB scale of brightness was used.

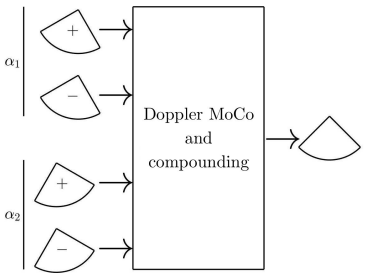

Fig. 6. MoCo C: Motion compensation is performed between all pulses directly, independently of the angle at which they were transmitted.

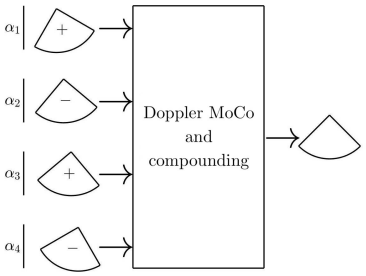

Fig. 7. Alternated contrast motion compensation scheme.

H. Evaluation metrics

1) Disc measurements

To validate the accuracy of simulation, the radii of the disc and cysts must be measured. To ensure no compounding or motion artefacts influence the measurements, they are performed directly on LRIs in a static condition. Measurements are performed by counting the number of pixels that belong to a certain region. The number of pixels can be converted to centimeters, since the dimensions of the pixels corresponds to the dimensions of grid points used in beamforming, which are known.

MATLAB has a built-in function which makes measurements easier, the `drawcircle` function. By providing one image and the corresponding sizes, in centimeters, of the depth and lateral axes, one can manually draw a circle on top of the region to be measured, and the radii is automatically computed given the size of the FOV.

2) Contrast-to-noise ratio

Contrast-to-noise ratio is used to evaluate the level of contrast between regions of different echogeneity. In the case of the rotating disc with anechoic inclusions, CNR is computed between the region of the disc and the region of the cysts. The equation used for computation of CNR is the one presented below:

$$\text{CNR (dB)} = 20 \log_{10} \frac{|\mu_{cyst} - \mu_{disc}|}{\frac{1}{2}\sqrt{\sigma_{cyst}^2 + \sigma_{disc}^2}} \tag{7}$$

where μ represents the mean in the region and σ the standard deviation in the same region.

To ensure a fair estimation of CNR, the contrast between the cysts and the disc must be evaluated in regions with the same total area. The map for computation of CNR is shown in Figure 8.

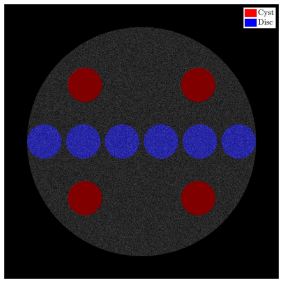

Fig. 8. Location map for computation of CNR. The red regions correspond to the cysts and the blue regions correspond to the disc.

CNR is computed between each cyst and the six disc regions across the lateral dimension, generating a total of 24 CNR measurements, for which the mean is taken. Since signal loss occurs along the lateral direction due to the higher axial velocities, measuring the CNR along multiple regions is more sensible than choosing a region in the center, for example.

3) Lateral evaluation of loss of intensity

In a rotating disc, since the axial velocity increases in the lateral direction, a way to evaluate loss of signal intensity with increasing velocity is by evaluating the mean intensity in the disc in the lateral axis. To perform this, the lines of the image corresponding to the disc are averaged in the depth direction. For each image line, one point of mean intensity intensity is obtained. The points are plotted according to their location in the lateral axis, producing a mean plot of mean lateral intensity.

4) Doppler velocity maps

Using the Doppler equation 4, the velocity of the disc can be evaluated at all points in space. The normalized mean square error was computed between the estimated velocity profiles and the theoretical, normalizing considering the theoretical maximum axial velocity in the disc.

III. Results

A. Disc and cyst measurements

The disc and cysts were measured according to section II-H1. Measurements were performed for all acquisitions in static condition for the disc, the top cysts and the bottom cysts across all LRIs. The percent differences in relation to the real dimensions were calculated and are presented in Table III:

TABLE III
MEAN RADII MEASUREMENTS OF THE DISC AND CYSTS IN DIFFERENT SIMULATION CONDITIONS. MEASUREMENTS IN CENTIMETERS.

	Frequency	Disc	Top Cysts	Bottom Cysts
AM	1.25 MHz	0.32 %	17.33 %	9.33 %
	1.75 MHz	0.24 %	14.40 %	6.40 %
	2.50 MHz	0.16 %	12.27 %	1.33 %
PI	1.25 MHz	0.12 %	13.07 %	1.07 %
	1.75 MHz	0.04 %	5.07 %	0.80 %
	2.50 MHz	0.00 %	1.60 %	0.27 %

B. Angled multipulse contrast motion compensation

The rotating disc phantom acquired with an angled multipulse PI/AM sequence was motion compensated with schemes A, B and C. Figures 9 and 10 show the images after envelope detection and log-compression for MultiAM and MultiPI, respectively. The first column of images represent the static disc, for which no compensation was performed. The second, third and fourth columns represent the moving disc compensated with MoCo schemes A, B and C, respectively. The fifth column shows the same moving disc with no motion compensation applied. The static and uncompensated images serve as controls. Each row in the figure represents an acquisition using a certain transmit frequency.

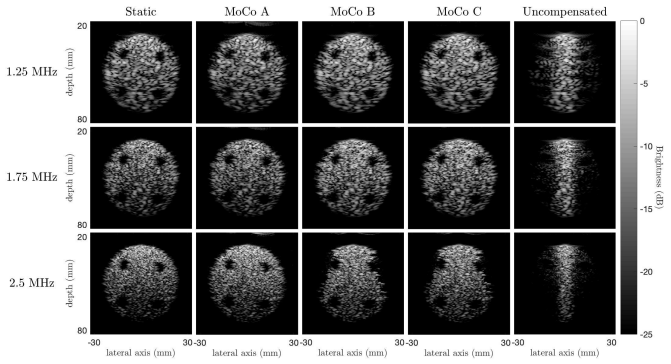

Fig. 9. Motion compensation in a rotating disc acquired using a MultiAM contrast sequence at multiple transmit frequencies.

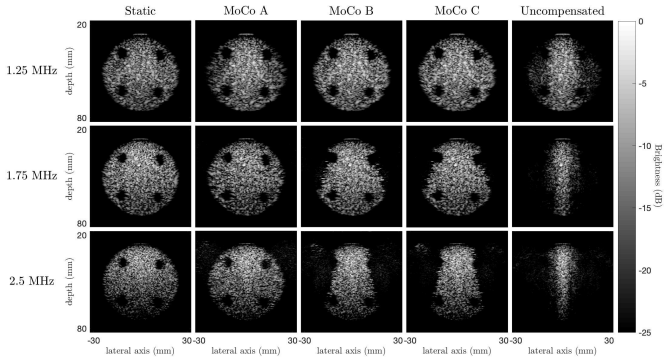

Fig. 10. Motion compensation in a rotating disc acquired using a MultiPI contrast sequence at multiple transmit frequencies.

Figure 11 shows the computed CNRs for all simulated cases in the form of a bar chart. There are six groups of bars, one for each combination of frequencies and contrast modes (MultiPI/MultiAM). For each group, five CNR bars are presented. From left to right, these are: Static, MoCo A, MoCo B, MoCo C and Uncompensated.

Lateral intensity loss/recovery was evaluated and results are presented in Figure 12. Each row of plots represents a transmit frequency - from top to bottom, 1.25 MHz, 1.75 MHz and 2.5 MHz - and each columns represents a contrast mode - MultiAM on the left and MultiPI on the right. Each subplot includes the mean lateral intensity of the static condition, motion compensated conditions A, B and C, and the uncompensated condition.

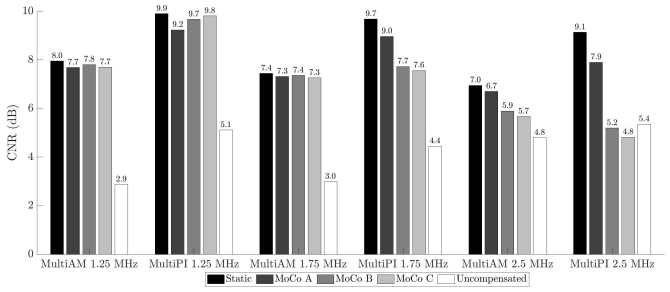

Fig. 11. CNR measurements in angled multipulse contrast mode for the static condition, motion compensated conditions A,B and C, and the uncompensated condition at multiple transmit frequencies.

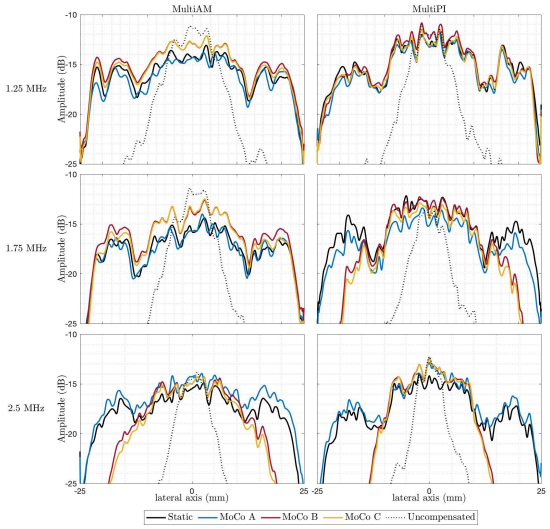

Fig. 12. Mean lateral intensity in angled multipulse contrast mode for the static condition, motion compensated conditions A,B and C, and the uncompensated condition at multiple transmit frequencies.

C. Alternated contrast motion compensation

Using an alternated contrast sequence, several acquisitions using different transmit frequencies were performed. Similarly to Figures 9-10 for the angled multipulse contrast sequence, Figures 13-14 shows the finalized images for the alternated contrast mode in the static condition, the motion compensated condition and the uncompensated condition.

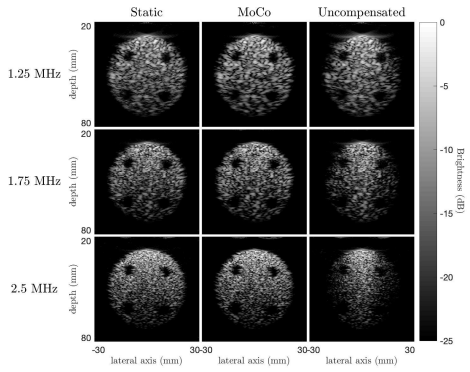

Fig. 13. Motion compensation in a rotating disc acquired using an alternated contrast sequence at multiple transmit frequencies.

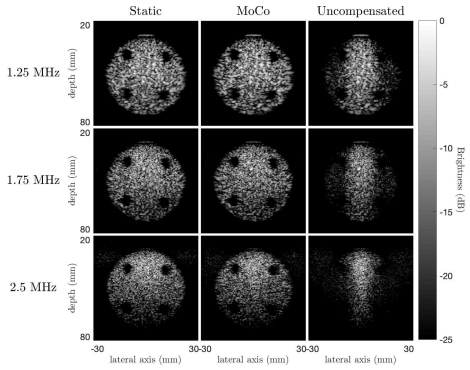

Fig. 14. Motion compensation in a rotating disc acquired using an alternated contrast sequence at multiple transmit frequencies.

CNR measurements for the alternated contrast sequences were performed the same way as the angled multipulse contrast sequences. Thus, the results presented in Figure 15 are analogous to the results presented in Figure 11.

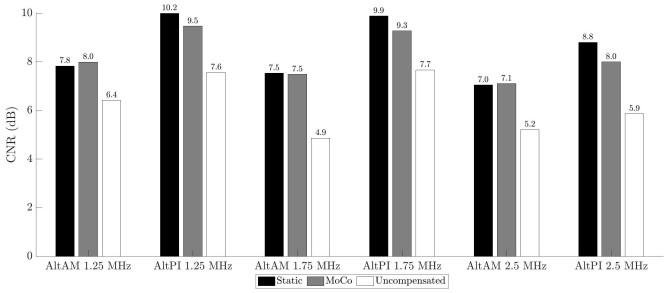

Fig. 15. CNR measurements in alternated contrast mode for the static condition, motion compensated condition, and the uncompensated condition at multiple transmit frequencies.

Similarly, lateral evaluation of loss/recovery of intensity shown in Figure 16 for the alternated contrast sequences is analogous to the results presented in Figure 12 for the angled multipulse contrast sequences.

D. Doppler velocity maps

The rotating disc velocity maps computed with the Doppler equation, 4, are shown in Figure 17 for all motion compensation methods explored - all three methods in angled multipulse contrast and the one method in alternated contrast, with both PI and AM transmissions at three different transmit frequencies.

The percent normalized root mean square errors computed in reference with the theoretical velocity profiles are presented in Table IV:

IV. Discussion

A. Simulation accuracy and validation

The results which will provide a baseline for evaluation of simulation accuracy and subsequent validation will be the measurements of the disc and cysts in Table III, and the images in Figures 9 - 10 and 13 - 14 corresponding to the static disc. These should resemble the sound speed map phantom shown in Figure 1.

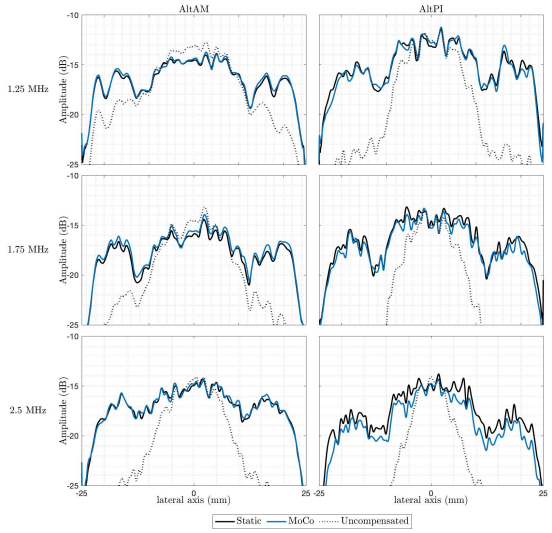

Fig. 16. Mean lateral intensity in alternated contrast mode for the static condition, motion compensated condition, and the uncompensated condition at multiple transmit frequencies.

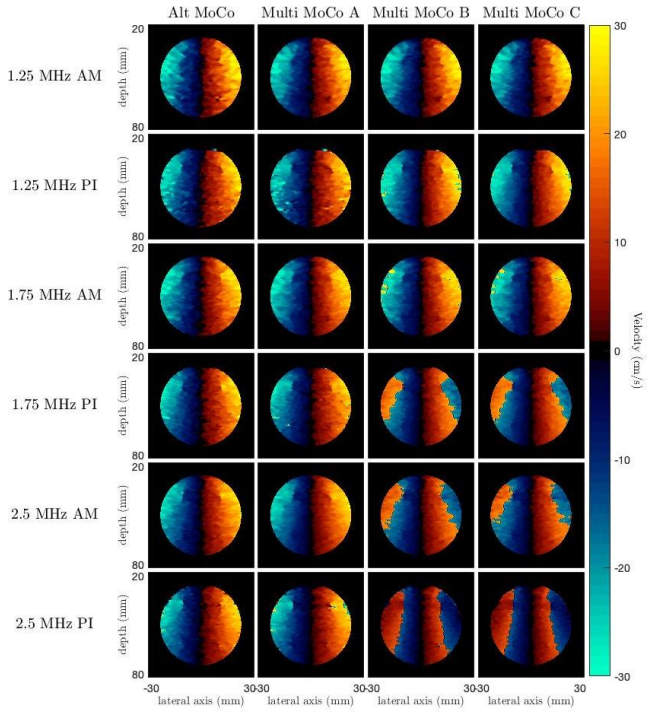

Fig. 17. Axial velocity profiles for different transmit frequencies, contrast modes and motion compensation methods.

The dimensions and location of the disc match the medium phantom with deviations from the real value lower than 1 %. However, the dimensions of the cysts have varying errors depending on the conditions of the simulation. In fact, the relative errors in the dimension of the cysts seem to decrease with increasing transmit frequency, are lower for the bottom cysts and are also lower in PI when compared to AM. All three of these factors can be explained by the effect of sidelobes. Sidelobe signal is generated most prominently in boundaries between regions with large differences in echogeneity, which is the case in the disc/cyst boundary. Figure 9 support this hypothesis, as some sidelobe signal from the disc can be seen ”bleeding” into the cyst region, mainly in the lateral direction. This explains why the bottom cysts' radius suffer less from this effect and their measurements are closer to reality. Sidelobe signals are weaker than mainlobe signals, and just like mainlobe signals these are attenuated as they propagate [19]. An already weak signal like the sidelobe is greatly attenuated as it reaches the depth of the lower cysts, so much so that the dynamic range of -25 dB is not enough for it to appear in the image. Furthermore, attenuation also increases with the transmit frequency, hence why the errors at larger frequencies are smaller, and why errors in PI are smaller than errors in AM - PI uses the 2^{nd} harmonic frequency, so for the same transmit frequency, the imaged frequency in PI is double the imaged frequency in AM.

TABLE IV
NRMSE OF THE DOPPLER VELOCITY MEASUREMENTS IN ALL SIMULATIONS.

	Alt	Multi A	Multi B	Multi C
1.25 MHz AM	5.44 %	5.53 %	4.94 %	4.97 %
1.25 MHz PI	6.48 %	9.73 %	12.79 %	8.99 %
1.75 MHz AM	4.52 %	4.34 %	14.13 %	12.63 %
1.75 MHz PI	5.07 %	6.89 %	41.51 %	41.42 %
2.50 MHz AM	4.44 %	4.16 %	40.63 %	38.72 %
2.50 MHz PI	8.97 %	15.25 %	42.04 %	41.70 %

From the static images, it is clear that the image brightness is higher at lower depths and lower at higher depths. This is a result of ultrasound signal attenuation. A property of ultrasound signal attenuation is that it is frequency dependent: the larger the frequency, the larger the attenuation [20]. Consider the static rows in Figure 9. As the frequency increases, the brightness of the images is lower at the same depth, illustrated by the intensity of each image at the bottom of the disc (highest for 1.25 MHz, lowest for 2.5 MHz). This effect is also visible in the PI images in Figure 10.

Another property of images acquired with ultrasound that is frequency dependent is the resolution [21]. Again, by analysing the static case in Figures 9 and 10, it is apparent that single scatterers are more easily resolved for the higher frequencies. Specifically, the resolution of PI images is always higher than AM images at the same transmit frequency due to the usage of the second harmonic.

Taking now attention to the uncompensated rotating disc images in Figures 9 and 10, it is observed that image intensity is lost at the edges of the disc and maintained in the center. This is in line with motion studies performed with similar in-vitro phantoms [10, 12]. Since the axial velocity increases laterally from the center, the regions where loss of intensity is higher are the regions where the axial velocity is higher - the lateral edges of the disc.

B. Overview of angled multipulse contrast motion compensation

The MultiAM/MultiPI sequences for HFR CEUS provide three distinct ways of compensating motion, which are now discussed.

From Figures 9 and 10, one finds that the images compensated using all three methods yield similar motion compensation results for 1.25 and 1.75 MHz in MultiAM and 1.25 MHz in MultiPI. For the higher frequencies in the corresponding contrast method, significant motion artefacts can be observed in images compensated with MoCo B and C, while the MoCo A scheme remains robust independent of frequency. This phenomenon is most easily observed in Figure 12, where the mean lateral intensity is plotted. It is clear that at 2.5 MHz in MultiAM and 1.75-2.5 MHz in MultiPI the lateral intensity nearer the edges is not recovered for MoCo B/C, while the lateral intensity profile of MoCo A is very similar to the static disc.

The phenomenon that leads to poor intensity recovery in MoCo schemes B and C is Doppler aliasing. This phenomeon is characterized by a "wrapping around" of the estimated velocities. To better illustrate how it occurs, consider the Doppler autocorrelator in its complex exponential form:

$$r_D(x,z) = |r_D(x,z)|e^{j\phi_D(x,z)} \tag{8}$$

The phase of the autocorrelator has values in the interval $[-\pi, \pi]$. The Doppler velocity equation can be rewritten in terms of the wavelength, by making the substitution $\lambda = c/f_0$:

$$v_D = \frac{c\mathrm{PRF}\phi_D}{4\pi f_0} = \frac{\mathrm{PRF}\phi_D\lambda}{4\pi} \tag{9}$$

The previous equation is maximized when the Doppler phase is $\phi_D = \pi$:

$$v_{D\max} = \frac{\mathrm{PRF}\lambda}{4} \tag{10}$$

Or, in terms of the displacement, $u_D = v_D/\mathrm{PRF}$:

$$u_{D\max} = \frac{\lambda}{4} \tag{11}$$

Equation 11 highlights the physical limits of the Doppler autocorrelator as a phase-domain method. It tells us that displacements larger than a fourth the wavelength within one pulse repetition period are not susceptible to be correctly estimated by the Doppler autocorrelator. When that happens, the estimated phase surpasses π, and thus wraps around due to the periodicity of the complex exponential in equation 8.

Due to this wrapping around effect of Doppler aliasing, aliasing is easily identifiable in the velocity maps in Figure 17 by looking for large discontinuities. In fact, large discontinuities can be found in the velocity maps of the images where lateral intensity recovery is poor, as initially postulated.

Since the maximum Doppler velocity decreases with frequency, the effects of aliasing become more drastic as frequency increases. Doppler aliasing leads to destructive sums since each LRI is often compensated according to velocities in the opposite direction of the actual motion, further contributing to incoherence.

Why does aliasing occur in MoCo B and C but not in MoCo A? In MoCo A, motion is estimated directly between all the consecutive pulses, while in MoCo B/C that is not the case. In MoCo B, the LRIs corresponding to the coded transmission are corrected first, and only then is correction performed between the angled transmissions. After compensation of the coded transmissions, one LRI per angle is obtained. Coded transmission is compensated using one of the pulses as a reference (the positive pulse for PI or the middle pulse for AM). Since this is performed for all angles, the obtained LRIs after the first stage of MoCo are equivalent to the corresponding postive pulse/middle pulse in its sequence. The time between transmission of two positive pulses in a PI sequence is $2/\mathrm{PRF}$, and two middle pulses is $3/\mathrm{PRF}$, so in essence the PRF is reduced for the second stage of MoCo.

Additionally, the MultiPI sequence aliases more drastically than the MultiAM sequence for the same transmit frequency. That is because the frequency at which MoCo is performed is the second harmonic for PI, further reducing the maximum Doppler velocity by a factor of 2. Note that the maximum Doppler velocity is further reduced by half by the usage of the two-autocorrelator approach combined with the triangular transmit sequence.

Contrary to MoCo schemes B and C, MoCo A keeps a high PRF by using a single motion compensation stage that estimates motion using all pulses in the sequence. No aliasing can be observed in the velocity maps of MoCo A in Figure 17. This leads to up to 5 dB higher lateral intensity recovery in MultiAM and up to 8 dB increases in MultiPI according to Figure 12. Moreoever, the CNR of MoCo A is 0.8/1 dB larger than aliased MoCo B/C, respectively in MultiAM, and 2.7/3.1 dB larger than aliased MoCo B/C, respectively in MultiPI.

While aliasing is the phenomenon that explain most of the observed differences between the MoCo schemes in MultiPI/AM, there are a few more observations that should be taken into account. More specifically, the number of LRIs that are used to estimate motion greatly influence the success of MoCo.

The expression for the measured velocity using the phase of the Doppler autocorrelator assumes infinite duration signals. In practice the signals used must have finite duration, but sufficiently good approximations can be achieved with a finite number of time points. The more time points are used, the closer the approximation will be. In this case, one time point corresponds to one transmitted pulse. It follows that the accuracy of Doppler MoCo increases with the number of pulses used for motion estimation.

MoCo A estimates motion between a total of 24 LRIs for PI and 36 for AM, while MoCo B estimates motion in the first stage between 2/3 pulses for PI/AM, respectively, and between 12 LRIs in the second stage for both. MoCo B estimates motion between only 12 LRIs. A few predictions can be gathered from these numbers directly: 1. Since MoCo A always used a larger number of pulses to estimate motion, it should compensate it more accurately than MoCo B/C; 2. Because the first MoCo stage of MoCo B uses a very small number of pulses for estimation, this step should result in almost negligible compensation; While it should compensate better than MoCo C, these methods should be very similar; 3. For MoCo A, compensation in MultiAM should be superior to compensation in MultiPI due to it using a larger number of pulses.

The first prediction is corroborated by the results of mean lateral intensity in Figure 12. The mean lateral intensity of MoCo A follows the static control more closely than the remaining methods. In the regions where aliasing does not occur, the lateral intensity of MoCo B and C are higher than MoCo C, but with larger differences from the static reference.

The second point is also verified in the lateral intensity recovery plots. The mean intensity of the discs compensated with MoCo B and C coincide across most of the lateral axis, with MoCo B being slightly closer to the static disc - differences no larger than 1 dB.

The third and final point is also verified: for the same transmit frequency, the mean lateral intensity of the disc compensated with MoCo A is closer to the static configuration in MultiAM when compared to MultiPI. This is also true for the CNR, as the differences in contrast are no larger than 0.3 dB across all frequencies in MultiAM, but can be as large as 1.2 dB in MultiPI.

To finalize the analysis of the angled multicontrast sequence, sidelobe suppression is noteworthy. Indeed, in the MultiAM acquisitions at 1.25 MHz and 1.75 MHz, large sidelobe signal can be observed at the top of the static discs, and to a lesser degree at the top of the static discs. These sidelobes are greatly suppressed during MoCo, especially when MoCo A is used. This is in agreement with Porée et al. (2016), who demonstrated that the usage of a two-autocorrelator approach in conjuction with a triangular transmit sequence greatly reduces sidelobes [10]. The presented results demonstrate that it still applies in CEUS. Furthermore, the obtained results show that the negative effects of sidelobes is generally reduced as the transmit frequencies increase. The 2.5 MHz AltAM sequence has barely visible sidelobes only in the uncompensated disc (on top) and top sidelobes are simply absent in AltPI acquisitions. [19].

C. Overview of alternated contrast motion compensation

The AltPI/AltAM sequences for HFR CEUS provides a way to compensate motion equivalent to non-contrast HFR ultrasound imaging.

In Figures 13 and 14, which show the contrast images in static, compensated and uncompensated conditions, we first turn our eyes to the uncompensated images. It is clear that loss of intensity is not as drastic compared to MultiPI/MultiAM. That can be attributed to the fact that a much smaller number of total pulses are used in AltPI/AltAM. The fewer the number of pulses, the less incoherence accumulates due to motion.

Similarly to MoCo A in MultiPI/MultiAM, the motion compensated discs are qualitatively very similar to the corresponding static ones, with approximately equal brightness distributions across the depth and the lateral axis for MultiAM. In MultiPI, despite the full disc being visible, small brightness discrepancies can be observed near the lateral edges of the disc between the static configuration and the compensated configuration.

The CNR comparisons provided in Figure 16 highlight the full contrast recovery of the motion compensated disc in AltAM, where the CNR of the MoCo disc are at least as high as the CNR in the static disc. In the AltPI acquisitions the contrast recovery is not total, with differences to the static disc ranging from 0.6 to 0.8 dB. However, the level of contrast that is recovered is on the order of 2 dB, when compared to the uncompensated discs. This level of recovery matches the level of recovery achieved in MultiAM in absolute terms, but since the base contrast of AltPI is up to 2 dB higher too, the recovered contrast in MultiPI is not as high relatively. The measured CNR of the alternated contrast sequences are on the same level of the angled multipulse contrast sequences despite the much smaller number of total transmitted pulses. This can be attributed to the fact that all pulses in AltPI/AltAM are acquired at a different angle. Pulses acquired with transmissions in slightly different directions further decorrelate noise distributions during compounding.

Figure 16 exhibits the mean lateral intensity for the AltPI/AltAM acquisitions. The plots corresponding to the motion compensated disc are almost coincident with the static disc, with the maximum observed differences to be around 1 dB (albeit rare) for all acquisitions except the 2.5 MHz AltPI one, which is the largest imaged frequency with the second harmonic at 5 MHz. This larger frequency is the one that is most attenuated, and thus the level of signal is the lowest of all acquisitions. As the signal decreases, the SNR increases, especially in PI since the second harmonic signal is weaker. This hypothesis can be is supported by the noise observable in the images of the AltPI acquisition at 2.5 MHz. Significant random noise is observed in the background region. Since the same level of noise was added to the phantom independently of location, it is expected that the same level of noise is present in the disc region, but it is harder to identify it. Noise can lead to imperfect motion estimation and ultimately motion artefacts with loss of intensity and contrast. Indeed, independently of the type of sequence used (angled multipulse contrast/alternated contrast), the CNR is consistently worse as the frequency increases. The mean lateral intensity of the motion compensated discs also increasingly deviate from the static disc as the transmit frequency increases. The frequency range at which the acquisitions were performed are too limited to gather any further conclusions about the poorer performance of the MoCo schemes with larger transmit frequencies. Further dedicated research on the topic with a wider range of frequencies is necessary to reach meaningful conclusions. High frequency ultrasounds have very limited applications due to their poor penetration, and thus comparative studies on the SNR of low and high frequency ultrasounds are still lacking.

On the topic of noise, it is important to note that the larger the number of pulses summed, the lower the level of noise due to averaging. Notably, despite the alternated sequence always having a smaller number of total pulses than the angled multipulse contrast sequence, the achieved contrast in AltPI/AltAM is on the same level of MultiPI/MultiAM, even in static conditions. This characteristic can be attributed to the fact that all AltPI/AltAM pulses are acquired at different angle, which is not the case for MultiPI/MultiAM. Acquiring all LRIs at a different angle ensures sidelobe incoherence across all pulses. The Doppler MoCo approach tends to rephase sidelobes [4, 10], so keeping them largely incoherent ensures

the intensity in the compensated image is as close as possible to the static image. Additionally, transmitting all pulses in different transmit angles further decorrelates random noise, improving the CNR and SNR [2, 22].

The measured axial velocities are in line with what is expected in a rotating disc phantom acquired with diverging wave transmissions. [10–12, 23]. The NRMSE of Doppler velocity estimates is always under 10%, and seems to decrease with frequency in AltAM, while no clear pattern can be seen in MultiPI. The NRMSE is also slightly lower in AM, highlighting the more accurate compensation in this mode, which is also line with the other evaluation metrics. It is worth noting that an 8.97 % NRMSE is oberved in AltPI at 2.5 MHz. This increased error arises from a very small degree of aliasing that occurs at that frequency. Using the Doppler velocity estimation limit in equation 10, and taking into account that this limit is halved by the usage of the two-autocorrelator approach, we determine that the maximum detectable velocity is 29.6 cm/s. Since the maximum velocity in the disc is in fact 30 cm/s, a very small level of aliasing occurs in this acquisition. For the same transmit frequency, an abnormally high error can also be observed in MultiPI, further corroborating this hypothesis.

The alternated contrast MoCo scheme bears many similarities with the MoCo approach by Porée et al. (2016), which was implemented in non-contrast mode with very positive results [10]. While compensating motion in contrast-mode presents more challenges than B-mode imaging, comparing the results of the two is still relevant, especially because the motion phantoms used are analogous. The achieved results are very similar - motion compensation was successful with intensity recovery across the entire lateral direction of the disc, axial velocity profiles congruent with the theoretical expectations, and contrast recovery close to the levels of the static case. The computed NRMSE are also extremely close. From this preliminary study with simulated data, we take that Doppler MoCo using contrast agents may thus be as accurate as Doppler MoCo in B-mode images if the transmissions sequences are optimized. Further investigation in in-vitro data is necessary to fully validate this methodolody.

D. Limitations

1) Limitations of simulation data

One of the biggest challenges in contrast-enhanced ultrasound imaging is the accurate modelling of microbubbles and their interactions. While many models relying on the Rayleigh-Plesset equation have been proposed to accurately describe asymmetric microbubble expansion, contraction and rupture in liquids [7, 24–26], the existing models are only able to model interactions of a single microbubble. The complexity of the existing models makes inter-microbubble interactions a very big challenge. Keeping this in mind, the best approximation that currently exists to simulate signal generating from microbubbles is the non-linear wave equations by adjusting the non-linearity parameter B/A to the measured values of microbubbles in high concentrations. While comparative studies of the accuracy of this approach in generating signals emulating microbubbles are lacking, the largely unpredictable behaviour of microbubbles leads us to believe that this methodology cannot fully grasp microbubble signal [27]. For this very reason, one must be cautious before making parallels between simulation data and real acquisitions in contrast-enhanced ultrasound imaging.

Another limitation of the simulation data is the fact that all simulations were carried out in two-dimensions. While ultrasound images are reconstructed to achieve a 2D dataset, acquisitions are carried out in 3D volumes. The presence of additional scatterer outside the imaging plane generates unwanted signal components which can reduce image quality. Additionally, the presence of out-of-plane motions provides an additional challenge for motion compensation [28, 29], and axial velocity Doppler methods are not suitable to compensate these types of motions [30].

2) Limitations of the motion compensation methods

While Doppler MoCo using axial velocity estimation can greatly reduce the prevalence of motion artefacts, there are several limitations to this approach.

The first and least important source of inaccuracy arises from the fact that only the axial component of the velocity is compensated, while the lateral component remains uncompensated. Full 2D MoCo provides an additional level of compensation, which can enhance coherence in compounding methods [12, 29, 31]. However, it has been extensively demonstrated that axial velocity estimation is sufficient to achieve accurate motion compensation [4, 10, 32].

The factor that does influence the results of MoCo tremendously is the average-motion estimation approach. The assumption that the velocity profile remains constant throughout the acquisition implies that Doppler methods estimate the average motion in a sequence of images. While this assumption is generally reasonable in most cases, it quickly breaks down in the presence of of rapidly changing motion patterns. One case where this occurs is echocardiography, where two distinct phases of motion of the heart can be considered - systole and diastole. To ensure that motion compensation is accurate in echocardiography, acquisitions must be performed synchronized with the heart beat, making sure that there is no overlap of the two phases of motion during a full angle sequence in the acquisition.

V. Conclusion

This work investigated unfocused ultrasound coded transmission sequences with the goal of optimizing Doppler motion compensation schemes in coherent compounding HFR CEUS.

Motion compensation was shown to be successful using the proposed transmission sequences in non-aliased conditions, with accurate estimated velocities and satisfactory intensity and contrast recovery.

In the future, the proposed methodology must be repeated in-vitro for a full validation on real data. If validation is successful, then the method can also be investigated in-vivo in contrast echocardiography or in fast blood flow studies.

ACKNOWLEDGMENT

This document was written and made publicly available as an institutional academic requirement and as a part of the evaluation of the MSc thesis in Biomedical Engineering of the author at Instituto Superior Técnico. The work described herein was performed at the Ultrasound Lab for Imaging and Sensing (ULIS) of Imperial College London (London, United Kingdom), during the period February-December 2020, under the supervision of Professor Mengxing Tang and Professor Rita Gouveia Nunes.

REFERENCES

[1] R. Smith-Bindman, M. L. Kwan, E. C. Marlow, M. K. Theis, W. Bolch, S. Y. Cheng, E. J. A. Bowles, J. R. Duncan, R. T. Greenlee, L. H. Kushi, J. D. Pole, A. K. Rahm, N. K. Stout, S. Weinmann, and D. L. Miglioretti. Trends in Use of Medical Imaging in US Health Care Systems and in Ontario, Canada, 2000-2016. *JAMA*, 322(9):843–856, 09 2019. ISSN 0098-7484. doi: 10.1001/jama.2019.11456.

[2] G. Montaldo, M. Tanter, J. Bercoff, N. Benech, and M. Fink. Coherent plane-wave compounding for very high frame rate ultrasonography and transient elastography. *IEEE Transactions on Ultrasonics, Ferroelectrics, and Frequency Control*, 56(3):489–506, 2009. doi: 10.1109/TUFFC.2009.1067.

[3] C. Papadacci, M. Pernot, M. Couade, M. Fink, and M. Tanter. High-contrast ultrafast imaging of the heart. *IEEE Transactions on Ultrasonics, Ferroelectrics, and Frequency Control*, 61(2):288–301, 2014. doi: 10.1109/TUFFC.2014.6722614.

[4] B. Denarie, T. A. Tangen, I. K. Ekroll, N. Rolim, H. Torp, T. Bjastad, and L. Lovstakken. Coherent plane wave compounding for very high frame rate ultrasonography of rapidly moving targets. *IEEE Transactions on Medical Imaging*, 32(7):1265–1276, 2013. ISSN 02780062. doi: 10.1109/TMI.2013.2255310.

[5] M. Toulemonde, W. C. Duncan, A. Stanziola, V. Sboros, Y. Li, R. J. Eckersley, S. Lin, M. Tang, and M. Butler. Effects of motion on high frame rate contrast enhanced echocardiography and its correction. In *2017 IEEE International Ultrasonics Symposium (IUS)*, pages 1–4, 2017. doi: 10.1109/ULTSYM.2017.8092362.

[6] A. Stanziola, M. Toulemonde, Y. O. Yildiz, R. J. Eckersley, and M. Tang. Ultrasound imaging with microbubbles [life sciences]. *IEEE Signal Processing Magazine*, 33(2):111–117, 2016. doi: 10.1109/MSP.2015.2496914.

[7] M.-X. Tang and R. J. Eckersley. Nonlinear propagation of ultrasound through microbubble contrast agents and implications for imaging. *IEEE transactions on ultrasonics, ferroelectrics, and frequency control*, 53 (12):2406–2415, 2006.

[8] M. Couade, M. Pernot, M. Tanter, E. Messas, A. Bel, M. Ba, A. Hagège, and M. Fink. Ultrafast imaging of the heart using circular wave synthetic imaging with phased arrays. In *2009 IEEE International Ultrasonics Symposium*, pages 515–518, 2009. doi: 10.1109/ULTSYM.2009.5441640.

[9] M. E. Toulemonde, R. Corbett, V. Papadopoulou, N. Chahal, Y. Li, C. H. Leow, D. O. Cosgrove, R. J. Eckersley, N. Duncan, R. Senior, and M.-X. Tang. High frame-rate contrast echocardiography: In-human demonstration. *JACC: Cardiovascular Imaging*, 11(6):923–924, 2018. doi: 10.1016/j.jcmg.2017.09.011.

[10] J. Poree, D. Posada, A. Hodzic, F. Tournoux, G. Cloutier, and D. Garcia. High-Frame-Rate Echocardiography Using Coherent Compounding with Doppler-Based Motion-Compensation. *IEEE Transactions on Medical Imaging*, 35(7):1647–1657, 2016. ISSN 1558254X. doi: 10.1109/TMI.2016.2523346.

[11] P. Joos, J. Porée, H. Liebgott, D. Vray, G. Cloutier, B. Nicolas, and D. Garcia. High-frame-rate velocity vector imaging echocardiography: An in vitro evaluation. *IEEE International Ultrasonics Symposium, IUS*, 2016-November, 2016. ISSN 19485727. doi: 10.1109/ULTSYM.2016.7728784.

[12] L. Nie, D. M. Cowell, T. M. Carpenter, J. R. McLaughlan, A. A. Cubukcu, and S. Freear. High Frame-Rate Contrast-Enhanced Echocardiography using Diverging Waves: 2-D Motion Estimation and Compensation. *IEEE Transactions on Ultrasonics, Ferroelectrics, and Frequency Control*, 66(2):359–371, 2018. ISSN 15258955. doi: 10.1109/TUFFC.2018.2887224.

[13] J. Wu and J. Tong. Measurements of the nonlinearity parameter ba of contrast agents. *Ultrasound in Medicine & Biology*, 24(1):153 – 159, 1998. ISSN 0301-5629. doi: https://doi.org/10.1016/S0301-5629(97)00207-X.

[14] L. Xia. Analysis of acoustic nonlinearity parameter b/a in liquids containing ultrasound contrast agents. *The Journal of the Acoustical Society of America*, 146(2):1394–1403, 2019. doi: 10.1121/1.5123486.

[15] W. Law, L. Frizzell, and F. Dunn. Determination of the nonlinearity parameter b/a of biological media. *Ultrasound in Medicine & Biology*, 11 (2):307 – 318, 1985. ISSN 0301-5629. doi: https://doi.org/10.1016/0301-5629(85)90130-9.

[16] T. L. Szabo. *Diagnostic ultrasound imaging: inside out*. Academic Press, 2004.

[17] B. Treeby, B. Cox, and J. Jaros. *k-Wave User Manual*. Available online at `http://www.k-wave.org`, 2016.

[18] B. E. Treeby, J. Jaros, A. P. Rendell, and B. Cox. Modeling nonlinear ultrasound propagation in heterogeneous media with power law absorption using ak-space pseudospectral method. *The Journal of the Acoustical Society of America*, 131(6):4324–4336, 2012.

[19] P. Y. Barthez, R. Léveillé, and P. V. Scrivani. Side lobes and grating lobes artifacts in ultrasound imaging. *Vet Radiol Ultrasound*, 38(5):387–393, Sep-Oct 1997. ISSN 1058-8183 (Print); 1058-8183 (Linking). doi: 10.1111/j.1740-8261.1997.tb02104.x.

[20] V. R. Amin. *Ultrasonic attenuation estimation for tissue characterization*. Digital Repository@ Iowa State University, http://lib. dr. iastate. edu/, 1989.

[21] A. Ng and J. Swanevelder. Resolution in ultrasound imaging. *Continuing Education in Anaesthesia, Critical Care & Pain*, 11:186–192, 09 2011. doi: 10.1093/bjaceaccp/mkr030.

[22] M. Correia, J. Provost, S. Chatelin, O. Villemain, M. Tanter, and M. Pernot. Ultrafast harmonic coherent compound (uhcc) imaging for high frame rate echocardiography and shear-wave elastography. *IEEE transactions on ultrasonics, ferroelectrics, and frequency control*, 63(3): 420–431, 2016.

[23] D. Posada, J. Porée, A. Pellissier, B. Chayer, F. Tournoux, G. Cloutier, and D. Garcia. Staggered multiple-prf ultrafast color doppler. *IEEE transactions on medical imaging*, 35, 01 2016. doi: 10.1109/TMI.2016.2518638.

[24] Q. Wang, K. Manmi, and M. L. Calvisi. Numerical modeling of the 3d dynamics of ultrasound contrast agent microbubbles using the boundary integral method. *Physics of Fluids*, 27(2):022104, 2015. doi: 10.1063/1.4908045.

[25] G. L. Chahine and C.-T. Hsiao. Modeling microbubble dynamics in biomedical applications. *Journal of Hydrodynamics*, 24(2):169–183, 2012.

[26] E. Stride and N. Saffari. Microbubble ultrasound contrast agents: a review. *Proceedings of the Institution of Mechanical Engineers, Part H: Journal of Engineering in Medicine*, 217(6):429–447, 2003.

[27] M.-X. Tang, H. Mulvana, T. Gauthier, A. Lim, D. Cosgrove, R. Eckersley, and E. Stride. Quantitative contrast-enhanced ultrasound imaging: a review of sources of variability. *Interface focus*, 1(4):520–539, 2011.

[28] S. Harput, K. Christensen-Jeffries, J. Brown, Y. Li, K. J. Williams, A. H. Davies, R. J. Eckersley, C. Dunsby, and M. X. Tang. Two-Stage Motion Correction for Super-Resolution Ultrasound Imaging in Human Lower Limb. *IEEE Transactions on Ultrasonics, Ferroelectrics, and Frequency Control*, 65(5):803–814, 2018. ISSN 08853010. doi: 10.1109/TUFFC.2018.2824846.

[29] A. Stanziola, M. Toulemonde, Y. Li, V. Papadopoulou, R. Corbett, N. Duncan, R. J. Eckersley, and M. X. Tang. Motion Artifacts and Correction in Multi-Pulse High Frame Rate Contrast Enhanced Ultrasound. *IEEE Transactions on Ultrasonics, Ferroelectrics, and Frequency Control*, 2018. ISSN 15258955. doi: 10.1109/TUFFC.2018.2887164.

[30] M. Toulemonde and M. X. Tang. Motion correction for high-frame-rate contrast enhanced echocardiography. *25th European Symposium on Ultrasound Contrast Imaging*, Rotterdam, 16-17 January, 2020.

[31] L. Nie, D. M. Cowell, T. M. Carpenter, J. R. McLaughlan, A. A. Cubukcu, and S. Freear. Motion Compensation for High-Frame-Rate Contrast-Enhanced Echocardiography Using Diverging Waves: Image Registration Versus Correlation-Based Method. *IEEE International Ultrasonics Symposium, IUS*, 2019-October:380–383, 2019. ISSN 19485727. doi: 10.1109/ULTSYM.2019.8925638.

[32] T. Loupas, J. Powers, and R. Gill. An axial velocity estimator for ultrasound blood-flow imaging, based on a full evaluation of the doppler equation by means of a 2-dimensional autocorrelation approach. *Ultrasonics, Ferroelectrics and Frequency Control, IEEE Transactions on*, 42:672 – 688, 08 1995. doi: 10.1109/58.393110.